Design of a swimming microrobot powered by a single piezoelectric bender

Cameron Urban[1*], Tyler King[2], Rafael Gottlieb[1], Hang Gao[1], and E. Farrell Helbling[3]

***Abstract*— Countless underwater robots seek to monitor aquatic environments while minimizing their impact on fragile ecosystems. At mm-scales, these systems can be used in a range of waterways, from shallow streams and rivers, to larger ponds and lakes, and navigate around large obstacles or through tight spaces in coral reefs, mangroves, or pipe systems. They can also be more readily used as platforms for biological study, as small-scale robots can more easily be integrated into bench-top characterization systems to verify hydrodynamic performance. Here, we present a new robotic platform, the Daniobot, a 16.5 mm body length (BL) microrobotic fish that is capable of achieving top speeds of 2.84 BL s^{-1}. At 23.8 mm total length (TL), Daniobot is, to the best of our knowledge, the smallest fish-inspired robot propelled by onboard actuators. We present the design, fabrication, and assembly of this robot as well as detailed position and velocity results at varying tail amplitudes and frequencies, and compare their trends to a simple analytical model. This design uses a single PZT bimorph actuator operating at 175 V, enabling future untethered experiments.**

I. Introduction

Aquatic environments are difficult to monitor and necessitate robotic solutions. Beyond autonomous underwater vehicles (AUVs), scientists and engineers draw inspiration from aquatic animals [1]–[3]. These robots can maneuver in more confined spaces and exhibit fin-based propulsion strategies that enable scientists to better understand the hydrodynamics of fish locomotion [4]. At the cm-scale, microrobotic swimmers can be used to monitor both natural (e.g., streams, rivers, and lakes) and engineered environments (e.g., pipes). Their high flapping frequencies and increased maneuverability can enable monitoring in confined spaces that larger robots cannot enter.

Many bio-inspired microrobotic (characteristic length $<$10 cm and total mass $<$5 g) swimmers have been developed in recent years [5]–[10]. These robots achieve fast locomotion (up to 8 BL s^{-1}) and are highly maneuverable, exhibiting turning radii of $\approx$7.6 cm [6]. Reducing the overall length can open up new applications in inspection of confined spaces, such as densely structured coral reefs or inside of nuclear reactor condenser coils (inner diameter $\approx$26 mm [11]). Similarly, we need a actuation strategy that is suitable for future autonomy, as a tethered robot, or one that relies on external magnetic fields [10], light [12], or local fuel [13] would be similarly unsuitable.

[1]Sibley School of Mechanical and Aerospace Engineering, Cornell University, Ithaca, NY, USA

[*]Corresponding Author cu49@cornell.edu

[2]Ann S. Bowers College of Computing and Information Science, Cornell University, Ithaca, NY, USA

[3]School of Electrical and Computer Engineering, Cornell University, Ithaca, NY, USA

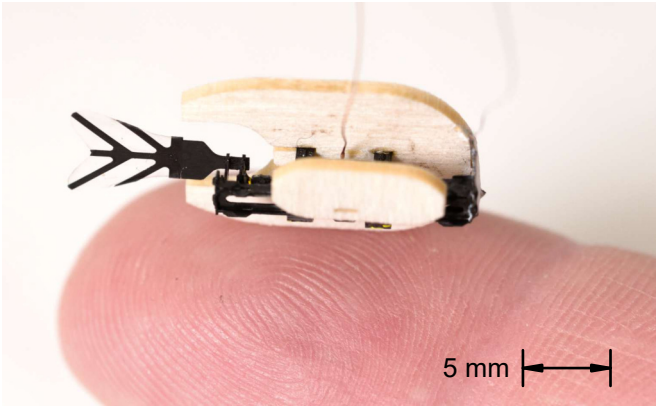


Fig. 1. Daniobot: a mm-scale fish-inspired microrobot powered by a single piezoelectric bender.

Here we present the design of the Daniobot (Fig. 1), named after the small freshwater fish, *Danio rerio*. The robot has a BL of 16.5 mm and a mass of 0.472 g. With a TL of 23.8 mm, Daniobot is, to our knowledge, the smallest fish-inspired robot propelled by onboard actuators. The robot is actuated using a single piezoelectric bimorph bender, and can achieve speeds up to 4.69 cm s^{-1} (2.84 BL s^{-1}) at an actuating voltage of 175 V, bested only by robots $>2\times$ its size. Additionally, we develop a simple analytical model for swimming speed versus frequency for systems driven near resonance, an operating regime chosen to maximize tail amplitude, and show that the model trends with experimental results. Although still tethered for electrical power, Daniobot's low driving voltage and high-efficiency actuator selection brings us one step closer to developing a power-autonomous mm-scale robotic fish.

The paper is organized as follows: Section II describes the mechanical design and fabrication of components, Section III details the robot assembly, Section IV discusses a simple analytical model for the robot's steady-state speed as a function of tailbeat frequency and amplitude, Section V discusses the experimental setup and data processing techniques, Section VI reports our initial results, and Section VII describes areas for further study.

II. Robot Design and Fabrication

To simplify the design, Daniobot performs ostraciiform locomotion, where a rigid tail oscillates at a single hinge point. To achieve this locomotion pattern, we utilize a piezoelectric bimorph actuator to generate an oscillating motion, a four-bar transmission to amplify this motion, a rigid tail, and a hydroframe to provide mechanical ground.

© 2025 IEEE. Personal use of this material is permitted. Permission from IEEE must be obtained for all other uses, in any current or future media, including reprinting/republishing this material for advertising or promotional purposes, creating new collective works, for resale or redistribution to servers or lists, or reuse of any copyrighted component of this work in other works. DOI: 10.1109/IROS60139.2025.11247311

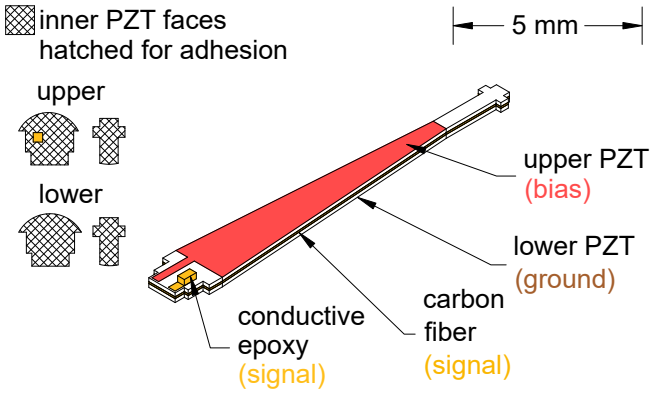


Fig. 2. The PZT bimorph actuator in this work is functionally similar to [14]. To enhance adhesion, we pattern a coarse hatching grid on the inner surfaces of the PZT plates at the tip extension and the base.

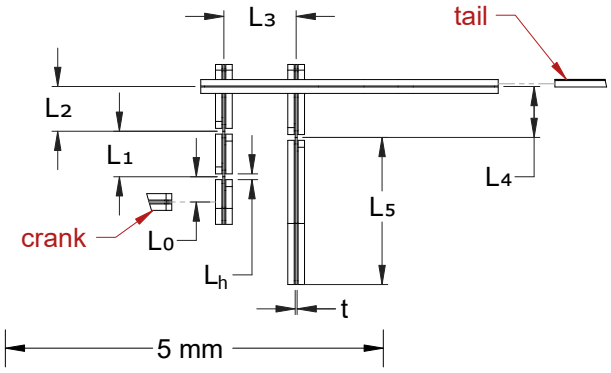


Fig. 3. Relevant dimensions L_0, L_1, and L_2, in the transmission-mount subassembly are shown on the transmission input, L_3 on the mount, and L_4 and L_5 on the transmission fulcrum. The thickness, t, and length, L_h, of the flexible layer are also shown on the input, and the same values are used for the flexible layer in the fulcrum.

A. Actuator Selection and Fabrication

Our robot uses a lead zirconate titanate (PZT) piezoelectric bimorph actuator due to its high power density [14], wide bandwidth, relatively low voltage requirements (compared to dielectric elastomer actuators and electrostatic actuators), and proven use in aquatic robots [6]–[9], [15]. By varying the frequency and amplitude of oscillation we can affect the speed of the robot. Finally, future iterations can integrate low-mass, high-efficiency step-up converters [16] for untethered locomotion.

Daniobot's actuator is comprised of upper and lower 127 µm-plates of PZT (piezo.com T105-H4NO-2929), with a central conductive layer of unilaminar carbon fiber prepreg (Toray Advanced Composites M55J RS-3C). We employed the streamlined fabrication process described in [14], with two modifications to prevent delamination between the central carbon fiber layer and the PZT. First, we increased the lamination pressure to 500 kPa, which had no visible damage to the PZT. Second, we patterned a coarse hatching grid with 45 µm spacing and 11 passes on the inner faces of the PZT plates using a UV laser cutter (LPKF ProtoLaser U4) to increase surface roughness and promote adhesion, as shown in Fig. 2.

To decrease manufacturing time, we removed the carbon fiber stiffening layers at the base and tip of the actuator. Stiffening elements were later added during the assembly process (described in Section III). Because we removed the carbon fiber stiffening elements, we also removed the copper layer that provides a reliable solder connection. We instead used conductive epoxy (MG Chemicals 8331D) to electrically connect the nickel traces and the corresponding signals on the actuator's printed circuit board (PCB), patterned on copper-clad FR4 (5 mil sheet). If the actuator needs to be disconnected from the PCB, the epoxy can be easily removed by heating.

To electrically isolate the actuator and PCB from the surrounding water, we coated the sides of the actuator with a thin layer of cyanoacrylate (CA) adhesive (Loctite 495) and insulated the entire subassembly (actuator and PCB) with a 9 µm layer of Parylene-C (Specialty Coating Systems Dichloro-p-cyclophane precursor) using a Parylene deposition machine (Specialty Coating Systems Model PDS 2010).

B. Flexure Design and Modeling

We designed a flexure-based transmission system to amplify the actuator displacement to the desired wing stroke profile. The transmission subassembly, depicted in Fig. 3, approximates the linear amplification of a first-class lever with a series of hinges. Using the Smart Composite Microstructures process, we can easily embed flexures between rigid links [17]. We chose the geometric link lengths $L_1 - L_5$ to provide a $\pm 18.1^\circ$ tail displacement at 175 V. The resonant frequency of the transmission subassembly is governed by the torsional stiffness of the flexure hinges, the mass of the tail, and the added-mass effect of the fluid accelerated by the tail during swimming. We created a model in MATLAB Simscape to predict and tune the resonant frequency of the system. The hinges have an angular stiffness (k in $\mathrm{N\,m\,rad^{-1}}$) as shown in Eq. 1 [18]:

$$k = \frac{Et^3 w}{12 L_h}, \tag{1}$$

where E is the elastic modulus (Pa), and t, w, and L_h are the flexures' thickness, width, and length, respectively (m). These flexures are connected by rigid elements (transmission links) in the Simscape model, to create the structural representative of the design shown in Fig. 3.

We used an approximate tail shape from an image of *D. rerio* as a starting point for our design, extracting the area and aspect ratio. We modeled the hydrodynamic force (F_n in N) on the tail tip where the normal velocity is highest:

$$F_n = \frac{C_n A_P \rho U_n^2}{2}, \tag{2}$$

where C_n is the dimensionless normal-force coefficient ($\approx$1.3 for a flat plate traveling perpendicular to a fluid [19]), A_P is the tail's projected area ($\mathrm{m^2}$), ρ is the fluid density ($\mathrm{kg\,m^{-3}}$),

and U_n is the normal component of the fluid velocity in the tail frame ($\mathrm{m\,s^{-1}}$).

We also included the added mass effect (m_A in kg) as follows:

$$m_A = C_A \rho V \tag{3}$$

where C_A is the dimensionless added-mass coefficient and V is the tail's volume ($\mathrm{m^3}$). For flat plates, this is commonly approximated as:

$$C_A = \frac{\pi w_{tail}}{4 d_{tail}} \tag{4}$$

where w_{tail} and d_{tail} are the tail's width and thickness (m) [20].

To compute the resonant frequency of the transmission subsystem, we simulated the position of the tail after an impulse response. Using the simulated parameters, we built an initial prototype to resonate in water at 12.5 Hz. During testing, we observed that the system resonated at ≈8 Hz, likely due to inaccurate approximations of the dimensionless numbers. We increased the added-mass coefficient by 2.5× the value calculated using Eq. 4 to match the observed resonant frequency.

To increase the frequency range of the robot [6], we decreased the tail area and increased the thickness and width of the flexure hinges until the resonant frequency in water was ≈30 Hz. The final geometry, shown in Fig. 3, has a tail area, A, of 28.5 $\mathrm{mm^2}$, and link lengths L_0 =0.334 mm, L_1 =0.602 mm, L_2 =0.592 mm, L_3 =0.956 mm, L_4 =0.674 mm, and L_5 =1.946 mm. The hinges have a width, w =1.671 mm, and a thickness, t =25.4 µm. As generally recommended for dynamic flexure hinges, we set their length, L_h to three times their thickness [18]. The transmission links are made of two carbon fiber laminates with thickness 85 µm (0-90-0 Toho Tenax QA-112) adhered to the central polyimide layer with acrylic sheet adhesive (DuPont Pyralux FR1500). During our swimming experiments, we measured the tail amplitude as 15.5° from the centerline at 175 V, which is fairly well matched to our model's prediction at this operating condition (18.1°).

C. Design and Fabrication of the Hydroframe, Tail Mount, and Tail

The tail mount is comprised of two carbon fiber laminates (0-90-0 Toho Tenax QA-112) adhered with an acrylic sheet adhesive. The upper layer has a series of castellations to mate with corresponding teeth on the tail. The tail is comprised of a 2.5 µm membrane (BoPET, Mylar, Premier Lab Supply TF-125) with carbon fiber stiffening elements (0-90-0 Toho Tenax QA-112).

The hydroframe is the mechanical skeleton of the Daniobot, which must mechanically ground the transmission and actuators, as well as resist bending and twisting. To minimize weight, we chose a hollow beam construction with two flanges on the top and bottom of the fish, which are rigidly connected to the frame and additional coupling features using a CA adhesive (Loctite 416), as discussed in the next section.

III. Assembly

For our initial prototype, we assemble the Daniobot in sequential steps, shown in detail in Fig. 4. In the first step, we secure the crank to the tip of the actuator subassembly (actuator and PCB) with epoxy (DEVCON 10 Minute Epoxy Clear Resin). The crank element rigidly connects along the entire length of the tip extension and provides an additional stiffening element to improve actuator performance. We then align the actuator subassembly (actuator, PCB, and crank) attach it to the hydroframe, which is composed of pre-assembled pieces of carbon fiber. Next, we attach the transmission input's first link (L_0) to the output link of the crank. Then, we attach the tail to the mount with UV-curing adhesive (Bondic), and connect the transmission fulcrum's first link (L_4). Next, we align the transmission input's L_2 link with the mount, joining the two subassemblies. Finally, we connect the transmission fulcrum's L_5 link to the hydroframe using one or more alignment shims. In the second step, we mechanically ground the base of the actuator with the carbon fiber actuator clip, which is attached using epoxy. In the third step, we attach the left and right basswood spines (Midwest Products, 0.031 25 in Basswood Sheets) to the hydroframe and add copper weights (McMaster-Carr 9014K178) to each of the eight balance points to properly align the CB and CG. In the final step, we attach a buoy to fix the robot depth during our experiments. The buoy is 3D printed (Prusa i3 MK3S+) using a filament containing a foaming agent to significantly reduce its density (colorFabb 1.75 mm LW-PLA). We attach the buoy to the hydroframe's using a strand of magnet wire (Remington Industries 36 AWG magnet wire). Finally, we connect a three-strand electrical tether (MWS Wire Multifilar Magnet Wire 3/50 HPN) to the PCB. To solder the wire to the PCB, we removed the layer of Parylene and then re-insulated the pads with a CA adhesive (Loctite 495). Unless noted otherwise, all components are connected using CA adhesive.

The Daniobot is unconstrained in six degrees of freedom; therefore, it is critically important to properly position the center of gravity (CG) and the center of buoyancy (CB). To prevent the body from rotating, the CG must be inline with all five external forces acting on the robot: gravity, tension from the post, buoyancy, thrust, and drag.

We place the post so that it coincides with the desired location of the robot's CG, which provides vertical support to the negatively-buoyant body without inducing a torque. We set the position of the spines such that the CB is placed slightly above the CG to provide a small degree of roll and pitch stability, as offsets in pitch and roll create a restoring moment. The vector connecting CB and CG is also parallel with the gravity vector. Finally, we align the thrust force by selecting a CG inline with the tail's neutral position. As drag forces act on every surface of the Daniobot, modeling the net force is nontrivial, so we chose to hand-tune the CG as necessary to compensate for any drag-induced rotation during experiments. We aligned the CG and CB and ensured that the robot was slightly negatively buoyant using Daniobot's CAD assembly (Onshape Educational Plan). To account for

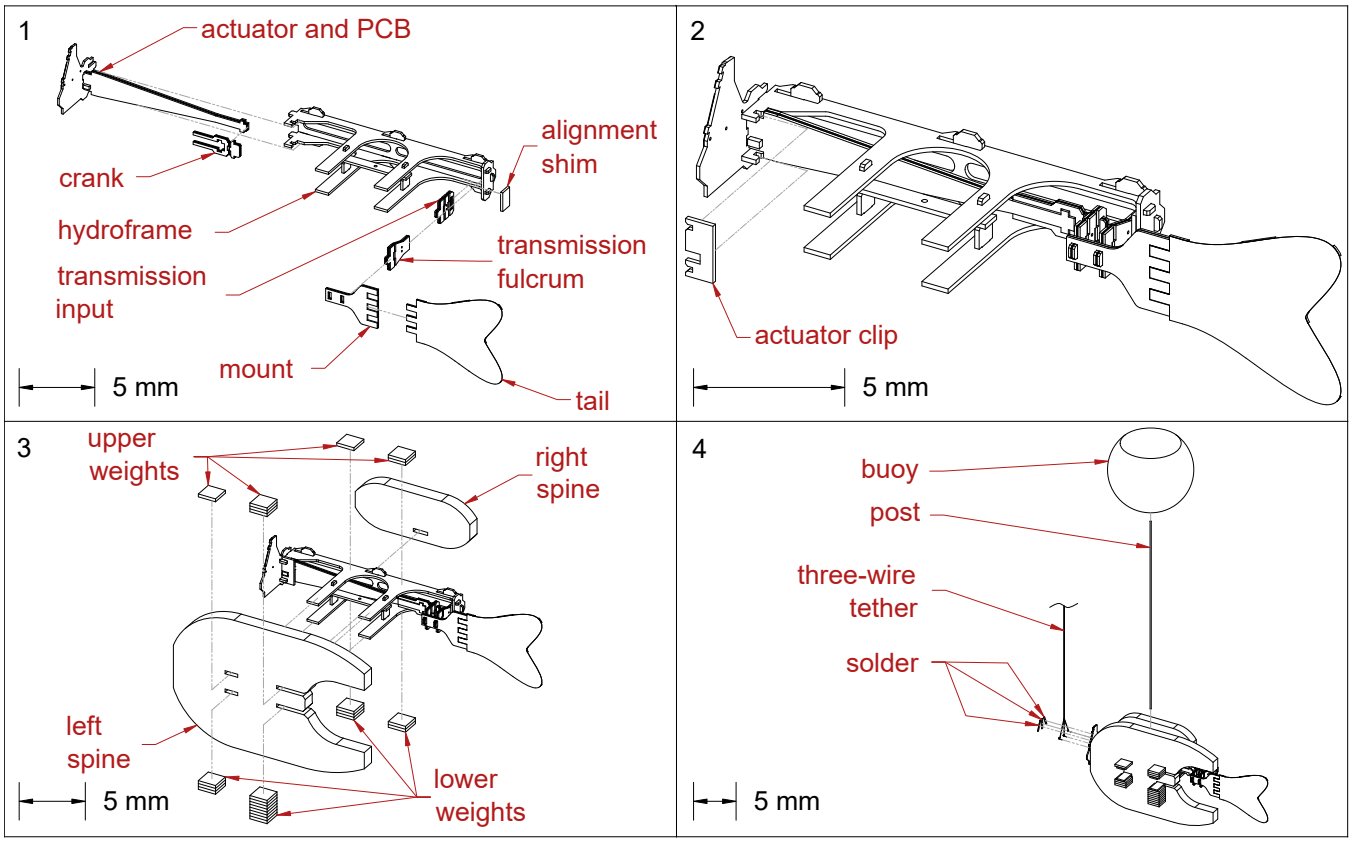


Fig. 4. The Daniobot assembly process.

any misalignments during assembly, we can add or remove weights from the hydroframe. The final robot weighs 0.472 g and has a TL of 23.8 mm.

IV. Analytical Modeling

The Daniobot has a Reynold's number of approximately $Re \approx 350$. In this regime, we can model the hydrodynamics with potential flow, simplifying the propulsive tail as a rectangular flat plate oscillating perpendicular to the freestream [21]. The steady-state swimming speed, U ($\mathrm{m\,s^{-1}}$) can be estimated using the following scaling law:

$$U = k_1 f (Ac)^{1/2}, \tag{5}$$

where k_1 is a unitless constant of proportionality, f is the tailbeat frequency (Hz), A is amplitude of the the tail's vertical travel (m), and c is half the tail's standard mean chord length (m). Because we are operating near the resonant frequency of our system, A is strongly dependent on f. We model the tail-transmission system as a spring-mass-damper with the following relationship:

$$A(f) = \frac{F_0}{\sqrt{(1-(f/f_n)^2)^2 + (2\zeta f/f_n)^2}}, \tag{6}$$

where F_0 is amplitude of the periodic force applied by the actuator (N) and ζ is the systems unitless damping ratio [22]. Then, substituting Eq. 6 into Eq. 5, we find the following relationship:

$$U(k_2, \zeta, f) = \frac{k_2 f \sqrt{c}}{((1-(f/f_n)^2)^2 + (2\zeta f/f_n)^2)^{1/4}}, \tag{7}$$

where $k_2 \equiv k_1\sqrt{F_0}$ ($\mathrm{N}^{1/2}$) is a constant. After substituting our known values for c and f_n, we use a nonlinear curve-fitting algorithm in MATLAB to find the values of k_2 and ζ that minimize the least-squares error of our model fit to our experimental data.

V. Experimental Setup

All experiments were performed in a high-clarity glass-bottomed tank (Ultum Nature Systems Ultra Clear Rimless Aquarium 16C) filled with deionized water (ChemWorld UltraPure type 1). We use an optical-quality mirror (Thorlabs ME8S-G01) to capture the in-plane motion of the robot. We add a small amount of surfactant to minimize bubble entrapment as the robot is lowered below the water's surface.

A. Testing

To characterize the robot's performance, we adjust the actuation voltage and frequency using an offboard power and control system (Speedgoat Baseline, Trek PZD350A) and use high-speed videography (Phantom VEO-710L) to record the $\mathrm{x}-\mathrm{y}$ position during experiments. To isolate effects of varying frequency and amplitude, each experiment tests one operating condition, defined as a tail amplitude and frequency pair. We tested frequencies of 5, 10, 15, 20, 25, and 30 Hz,

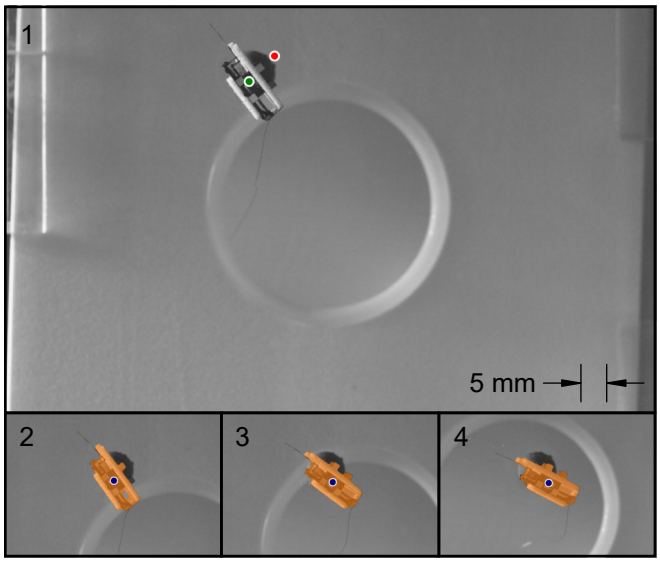


Fig. 5. Robot segmentation and tracking with SAM 2 [24]. (1) Positive (green) and negative (red) prompting points generate the preliminary segmentation mask on the first video frame. (2-4) Segmentation masks (orange) and mask centroids (black) obtained from SAM 2 at the start, midpoint, and end of the full amplitude stage.

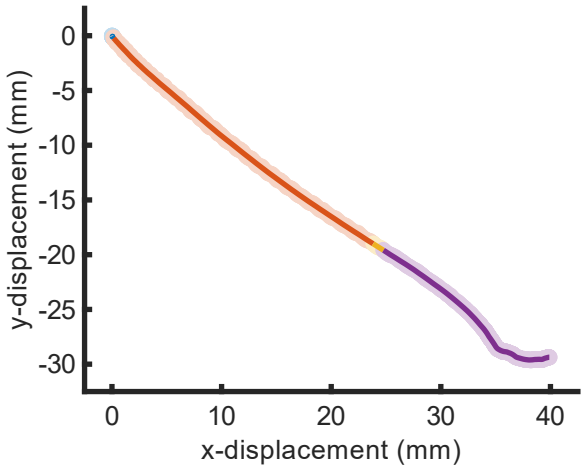


Fig. 6. Example robot trajectory at operating condition 30 Hz and 150 V. Filtered data (solid lines) are plotted on top of raw data (transparent points). The experiment consisted of four phases: (1) ramping up the amplitude from 0 V to 150 V over the course of five tail beats (shown in blue), (2) swimming with the full amplitude for 32 tail beats (shown in red), (3) ramping down the amplitude to 0 V (shown in yellow), and (4) coasting (shown in purple). The raw data points are displayed beneath the solid lines, which represent the trajectory smoothed with a third-order Savitzky–Golay filter with a window size equivalent to six tail beats.

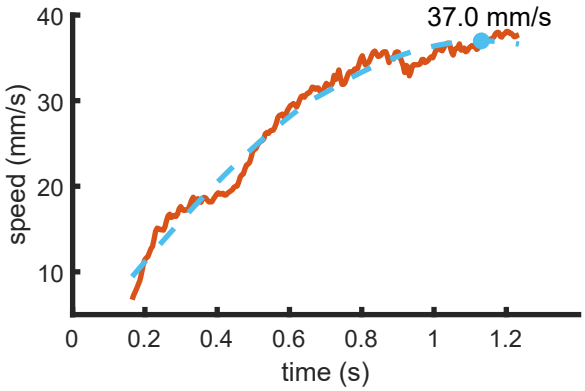


Fig. 7. Example maximum speed at operating condition 30 Hz and 150 V.

and voltages of 100, 125, and 150 V. For each of these 15 operating conditions, we repeated each experiment three times. Finally, we increased the operating voltage to 175 V and 30 Hz, to measure the maximum speed for the robot over two trials. We recorded data from all 47 experiments at a frame rate 100× each test's tail-beat frequency.

B. Data Extraction

To measure the robot position, we convert the video recording into a series of frames via FFmpeg [23]. Using the Segment Anything Model 2 (SAM 2) [24], we attain pixel-level segmentations of the Daniobot in experimental data. To initialize SAM 2, we annotate the first frame with positive (green) and negative (red) prompting points (see Fig. 5.1). We place the positive point near the Daniobot center of mass and the negative point (if needed) on the buoy. Points are then fed into an image-based SAM model [25], which outputs an initial segmentation mask.

SAM 2 then temporally propagates this mask through successive frames, achieving spatio-temporal masklets for the duration of the video. At each frame, the segmentation centroid is computed and converted into spatial coordinates (in mm) to determine Daniobot's $x-y$ position. Such masklets can be seen in Fig. 5.2-4, which displays the start, middle, and end of the full amplitude phase for a single recording.

C. Data Processing

We then plot the robot trajectory using the extracted $x-y$ position data. We use a third-order Savitzky-Golay filter with a window size of six tail beats so that we are able to track linear changes in acceleration and record the robot's average motion over multiple tail beats (see Fig. 6 for a representative example). Next, we compute the robot's instantaneous speed using the central difference method and take the Euclidean norm at each time step. We fit the data using a third-order polynomial and use the maximum estimated value to determine the robot's maximum speed, see Fig 7.

VI. Results and Discussion

As shown in Fig. 6, the robot is able to perform straight-line open-loop locomotion. The robot steadily accelerates until it reaches a near-constant velocity, at which point the drag on the robot's body balances the thrust produced by the tail. During the coasting phase, the robot continues following the straight-line trajectory until it slows to a stop. These results are expected given our careful tuning of Daniobot's CG and CB locations to ensure that no external forces create significant torque about the CG.

Figure 8 shows the average maximum velocity and standard error for each operating condition. As expected, robot speed

increases with voltage and frequency. However, we observe a reduction in speed at 25 Hz. Upon inspection, it appears that the buoy and post were twisting at higher amplitudes, indicating that we entered a dynamic regime of the buoy-post-body system, resulting in energy loss. Frequency appears to have a larger effect on speed and indicates that modifying frequency may be a promising method of control in future experiments. We measured maximum speeds of $(2.42 \pm 0.22)\,\mathrm{BL\,s^{-1}}$ at 30 Hz-150 V and $(2.84 \pm 0.09)\,\mathrm{BL\,s^{-1}}$ 30 Hz-175 V. This falls in a similar range to other fish-inspired microrobots, which typically obtain speeds $\approx 2\,\mathrm{BL\,s^{-1}}$, with some larger models obtaining a speeds up to $8.01\,\mathrm{BL\,s^{-1}}$ [6]–[8], [26]. However, the use of a buoy greatly reduces speed due to increased drag. This has been shown to decrease robot speed by as much as $4.3\times$ [6]. We expect significant improvement in velocity in future results without the stabilizing buoy.

Figure 8 also shows the results of fitting our non-linear analytical model from Section IV to the data at 100, 125, and 150 V, with r^2 values of 0.75, 0.77, and 0.84 respectively.

Along with the Reynolds number, the Strouhal number is of critical importance to comparing the unsteady fluid flows associated with swimming fish. Using the same operating condition as when calculating Reynolds number, we find that Daniobot's Strouhal number, calculated as $St = 2Af/U$, to be approximately 1.89, which falls outside the 0.42 to 1.28 range typically observed in *D. rerio* locomotion [27], and even further outside the 0.25 to 0.35 range classically considered optimal for thrust generation in fish-like swimming [28]. This indicates that there may be significant headroom for future work optimizing our design to improve its performance and efficiency.

VII. Conclusions and Future Work

This work describes the design, assembly, and characterization of a mm-scale microrobotic fish. This sub-gram fish can reach maximum speeds of $2.84\,\mathrm{BL\,s^{-1}}$, similar to pre-existing robotic designs. The robot is currently limited to straight-line locomotion. Preliminary turning experiments were attempted by adjusting the mean tail angle during flapping through adding a DC offset voltage to the sinusoidal drive signal. Small voltage changes appeared to have little effect on the turning angle, and we could not further increase the voltage without damaging the actuators. We predict that modifying the shape of the spine, eliminating the buoy, and adding additional passive and active control surfaces can increase robot maneuverability and provide depth control. To this end, we intend to expand the existing model to predict thrust and drag forces and investigate different turning strategies.

Furthermore, future work looks to integrate Daniobot with an off-the-shelf 330 mg lithium battery that has previously been integrated in a PZT-powered microrobot [29]. Then, implementing a modified version of the 90 mg drive circuit previously used Robobee [16] will allow us to achieve in the first untethered, controllable swimming of a sub-gram power autonomous microrobot.

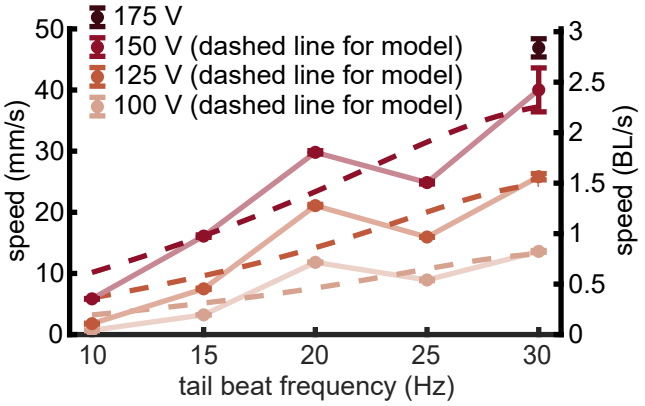


Fig. 8. Daniobot's swimming speed across its operating range of frequencies and voltage amplitudes. Error bars represent the standard error of the trials at each operating point. Only one frequency is shown for the 175 V amplitude, as the actuator shorted during the third trial at 30 Hz, before collecting data for the other frequencies. The body's length of 16.5 mm was used to plot the normalized speeds in $\mathrm{BL\,s^{-1}}$. Trends show the best fit approximation to the model in Eq. 7 for the 100, 125, and 150 V data.

Acknowledgment

This work was performed in part at the Cornell NanoScale Facility, an NNCI member supported by NSF Grant NNCI-2025233 and supported in part by the Office of Naval Research (N00014-24-1-2141-P00001). Any opinions, findings, and conclusions or recommendations expressed in this material are those of the author(s) and do not necessarily reflect the views of the Office of Naval Research.

References

[1] Y. Li, Y. Xu, Z. Wu, L. Ma, M. Guo, Z. Li, and Y. Li, "A comprehensive review on fish-inspired robots," *International Journal of Advanced Robotic Systems*, vol. 19, no. 3, p. 17298806221103707, 2022. [Online]. Available: https://doi.org/10.1177/17298806221103707

[2] X. Jian and T. Zou, "A review of locomotion, control, and implementation of robot fish," *Journal of Intelligent & Robotic Systems*, vol. 106, no. 2, p. 37, Sep. 2022. [Online]. Available: https://doi.org/10.1007/s10846-022-01726-w

[3] S. Ma, Q. Zhao, M. Ding, M. Zhang, L. Zhao, C. Huang, J. Zhang, X. Liang, J. Yuan, X. Wang, and G. He, "A review of robotic fish based on smart materials," *Biomimetics*, vol. 8, no. 2, p. 227, May 2023. [Online]. Available: https://www.mdpi.com/2313-7673/8/2/227

[4] X. Shi, Z. Chen, T. Zhang, S. Li, Y. Zeng, L. Chen, and Q. Hu, "Hydrodynamic performance of a biomimetic undulating fin robot under different water conditions," *Ocean Engineering*, vol. 288, p. 116068, Oct. 2023. [Online]. Available: https://www.sciencedirect.com/science/article/pii/S0029801823024526

[5] J. Ko, C. Kim, D. Kim, Y. Song, S. Lee, B. Yeom, J. Huh, S. Han, D. Kang, J.-S. Koh, and J. Cho, "High-performance electrified hydrogel actuators based on wrinkled nanomembrane electrodes for untethered insect-scale soft aquabots," *Science Robotics*, vol. 7, no. 71, p. eabo6463, Oct. 2022. [Online]. Available: https://www.science.org/doi/10.1126/scirobotics.abo6463

[6] J. Zhao, X. Gao, Y. Xiao, C. Wu, G. Wu, Z. Wang, Y. Zhang, F. Cui, and W. Liu, "A fish-like underwater miniature robot capable of high-speed and controllable locomotion," *IEEE Robotics and Automation Letters*, vol. 9, no. 4, pp. 3910–3917, Apr. 2024. [Online]. Available: https://ieeexplore.ieee.org/document/10457573

[7] Q. Zhao, S. Liu, J. Chen, G. He, J. Di, L. Zhao, T. Su, M. Zhang, and Z. Hou, "Fast-moving piezoelectric micro-robotic fish with double caudal fins," *Robotics and Autonomous Systems*, vol. 140, Jan. 2021. [Online]. Available: https://www.sciencedirect.com/science/article/pii/S092188902100018X?via%3Dihub

[8] R. Liu, Y. Wu, J. Jin, L. Wang, R. Qi, and P. Yu, "A biomimetic piezoelectric composite-driven undulation underwater robotic structure: characteristic analysis and experimental investigation," *Advanced Intelligent Systems*, vol. 5, no. 12, p. 2300357, 2023. [Online]. Available: https://onlinelibrary.wiley.com/doi/abs/10.1002/aisy.202300357

[9] J. Xu, J. Jin, L. Wang, R. Liu, J. Zhang, and Y. Wu, "Design, simulation, and experimental investigation on a novel robot fish driven by piezoelectric bimorphs," *Smart Materials and Structures*, vol. 32, no. 8, p. 085019, Jul. 2023. [Online]. Available: https://dx.doi.org/10.1088/1361-665X/ace010

[10] D. Wei, S. Hu, Y. Zhou, X. Ren, X. Huo, J. Yin, and Z. Wu, "A magnetically actuated miniature robotic fish with the flexible tail fin," *IEEE Robotics and Automation Letters*, vol. 8, no. 10, pp. 6099–6106, Oct. 2023. [Online]. Available: https://ieeexplore.ieee.org/document/10197493

[11] V. V. Nazarov and L. P. Zaekin, "Condensers of large steam turbines for thermal and nuclear power stations," *Thermal Engineering*, vol. 54, no. 10, pp. 828–835, Oct. 2007. [Online]. Available: https://doi.org/10.1134/S0040601507100114

[12] S.-J. Park, M. Gazzola, K. S. Park, S. Park, V. Di Santo, E. L. Blevins, J. U. Lind, P. H. Campbell, S. Dauth, A. K. Capulli, F. S. Pasqualini, S. Ahn, A. Cho, H. Yuan, B. M. Maoz, R. Vijaykumar, J.-W. Choi, K. Deisseroth, G. V. Lauder, L. Mahadevan, and K. K. Parker, "Phototactic guidance of a tissue-engineered soft-robotic ray," *Science*, vol. 353, no. 6295, pp. 158–162, Jul. 2016. [Online]. Available: https://www.science.org/doi/full/10.1126/science.aaf4292

[13] W. Zhu, J. Li, Y. J. Leong, I. Rozen, X. Qu, R. Dong, Z. Wu, W. Gao, P. H. Chung, J. Wang, and S. Chen, "3D-printed artificial microfish," *Advanced Materials*, vol. 27, no. 30, pp. 4411–4417, 2015. [Online]. Available: https://onlinelibrary.wiley.com/doi/abs/10.1002/adma.201501372

[14] N. T. Jafferis, K. Jayaram, P. A. York, and R. J. Wood, "A streamlined fabrication process for high energy density piezoelectric bending actuators," *Sensors and Actuators: A. Physical*, vol. 332, p. 113155, Oct. 2021. [Online]. Available: https://www.sciencedirect.com/science/article/pii/S0924424721006208

[15] Y. Chen, H. Wang, E. F. Helbling, N. T. Jafferis, R. Zufferey, A. Ong, K. Ma, N. Gravish, P. Chirarattananon, M. Kovac, and R. J. Wood, "A biologically inspired, flapping-wing, hybrid aerial-aquatic microrobot," *Science Robotics*, vol. 2, no. 11, p. eaao5619, Oct. 2017. [Online]. Available: https://www.science.org/doi/10.1126/scirobotics.aao5619

[16] "Untethered flight of an insect-sized flapping-wing microscale aerial vehicle," vol. 570, pp. 491–495, 2019. [Online]. Available: https://www.nature.com/articles/s41586-019-1322-0

[17] J. P. Whitney, P. S. Sreetharan, K. Y. Ma, and R. J. Wood, "Pop-up book MEMS," *Journal of Micromechanics and Microengineering*, vol. 21, no. 11, p. 115021, Oct. 2011. [Online]. Available: https://dx.doi.org/10.1088/0960-1317/21/11/115021

[18] F. Ramirez Serrano, E. Steinhardt, and R. J. Wood, "Considerations for the design and rapid manufacturing of pop-up MEMS devices," *Advanced Materials Technologies*, p. 2301940, 2024. [Online]. Available: https://onlinelibrary.wiley.com/doi/abs/10.1002/admt.202301940

[19] N. Hall, "Shape effects on drag," Jun. 2024. [Online]. Available: https://www1.grc.nasa.gov/beginners-guide-to-aeronautics/shape-effects-on-drag-2/

[20] M. Denny, *Ecological mechanics: Principles of life's physical interactions*. Princeton University Press, 2016.

[21] S. Jung, "Swimming, flying, and diving behaviors from a unified 2D potential model," *Scientific Reports*, vol. 11, no. 1, p. 15984, 2021. [Online]. Available: https://www.nature.com/articles/s41598-021-94829-7

[22] L. Meirovitch, *Fundamentals of vibrations*. Boston: McGraw-Hill, 2001.

[23] S. Tomar, "Converting video formats with FFmpeg," *Linux Journal*, vol. 2006, no. 146, p. 10, Jun. 2006.

[24] N. Ravi, V. Gabeur, Y.-T. Hu, R. Hu, C. Ryali, T. Ma, H. Khedr, R. Rädle, C. Rolland, L. Gustafson, E. Mintun, J. Pan, K. V. Alwala, N. Carion, C.-Y. Wu, R. Girshick, P. Dollár, and C. Feichtenhofer, "SAM 2: Segment anything in images and videos," Oct. 2024. [Online]. Available: http://arxiv.org/abs/2408.00714

[25] A. Kirillov, E. Mintun, N. Ravi, H. Mao, C. Rolland, L. Gustafson, T. Xiao, S. Whitehead, A. C. Berg, W.-Y. Lo, P. Dollár, and R. Girshick, "Segment anything," Apr. 2023. [Online]. Available: http://arxiv.org/abs/2304.02643

[26] Q. Zhao, J. Chen, H. Zhang, Z. Zhang, Z. Liu, S. Liu, J. Di, G. He, L. Zhao, M. Zhang, T. Su, and X. Liang, "Hydrodynamics modeling of a piezoelectric micro-robotic fish with double caudal fins," *Journal of Mechanisms and Robotics*, vol. 14, no. 034502, Dec. 2021. [Online]. Available: https://doi.org/10.1115/1.4052973

[27] T. Han, G. Lombardelli, S. D. Peterson, and M. Porfiri, "Inferring the metabolic rate of zebrafish from ventilation frequency," *Journal of Fish Biology*, vol. 105, no. 6, pp. 1939–1950, Aug. 2024. [Online]. Available: https://onlinelibrary.wiley.com/doi/abs/10.1111/jfb.15922

[28] G. S. Triantafyllou, M. S. Triantafyllou, and M. A. Grosenbaugh, "Optimal thrust development in oscillating foils with application to fish propulsion," *Journal of Fluids and Structures*, vol. 7, no. 2, pp. 205–224, 1993. [Online]. Available: https://www.sciencedirect.com/science/article/pii/S0889974683710121

[29] B. Goldberg, R. Zufferey, N. Doshi, E. F. Helbling, G. Whittredge, M. Kovac, and R. J. Wood, "Power and control autonomy for high-speed locomotion with an insect-scale legged robot," *IEEE Robotics and Automation Letters*, vol. 3, no. 2, pp. 987–993, 2018. [Online]. Available: https://ieeexplore.ieee.org/abstract/document/8258869/